LETTER

Evidence for a spinon Fermi surface in a triangular–lattice quantum–spin–liquid candidate

Yao Shen[1], Yao-Dong Li[2], Hongliang Wo[1], Yuesheng Li[3], Shoudong Shen[1], Bingying Pan[1], Qisi Wang[1], H. C. Walker[4], P. Steffens[5], M. Boehm[5], Yiqing Hao[1], D. L. Quintero-Castro[6], L. W. Harriger[7], M. D. Frontzek[8], Lijie Hao[9], Siqin Meng[9], Qingming Zhang[3,10,11], Gang Chen[1,11,12] & Jun Zhao[1,11]

A quantum spin liquid is an exotic quantum state of matter in which spins are highly entangled and remain disordered down to zero temperature. Such a state of matter is potentially relevant to high-temperature superconductivity and quantum-information applications, and experimental identification of a quantum spin liquid state is of fundamental importance for our understanding of quantum matter. Theoretical studies have proposed various quantum-spin-liquid ground states[1–4], most of which are characterized by exotic spin excitations with fractional quantum numbers (termed 'spinons'). Here we report neutron scattering measurements of the triangular-lattice antiferromagnet YbMgGaO$_4$ that reveal broad spin excitations covering a wide region of the Brillouin zone. The observed diffusive spin excitation persists at the lowest measured energy and shows a clear upper excitation edge, consistent with the particle–hole excitation of a spinon Fermi surface. Our results therefore point to the existence of a quantum spin liquid state with a spinon Fermi surface in YbMgGaO$_4$, which has a perfect spin-1/2 triangular lattice as in the original proposal[4] of quantum spin liquids.

In 1973, Anderson[4] proposed the idea of a quantum spin liquid (QSL) in the study of the triangular-lattice Heisenberg antiferromagnet. This idea was revived after the discovery in 1986 of high-temperature superconductivity[5]. A QSL, as currently understood, does not fit into Landau's conventional paradigm of symmetry-breaking phases[1,2,6,7], and is instead an exotic state of matter characterized by spinon excitations and emergent gauge structures[1–3,6]. The search for QSLs in models and materials[8–12] has been partly facilitated by the Oshikawa–Hastings–Lieb–Schultz–Mattis (OHLSM) theorem, which hints at the possibility of QSLs in Mott insulators with odd electron fillings and a global U(1) spin rotational symmetry[13–15]. Indeed, a continuum of spin excitations has been observed in the kagome-lattice material ZnCu$_3$(OD)$_6$Cl$_2$ (refs 12, 16). However, the requirement of the U(1) spin rotational symmetry prevents the application of the OHLSM theorem in strongly spin–orbit-coupled Mott insulators, in which the spin rotational symmetry is completely absent. A recent theory addressed this limitation of the OHLSM theorem, arguing that, as long as time-reversal symmetry is preserved, the ground state of a spin–orbit-coupled Mott insulator with odd electron fillings must be exotic[17].

The triangular antiferromagnet YbMgGaO$_4$ (refs 18, 19) displays no indication of magnetic ordering or symmetry breaking at temperatures as low as 30 mK, despite the energy scale for spin interaction being equivalent to a temperature of approximately 4 K. Because of the strong spin–orbit coupling of the Yb electrons, YbMgGaO$_4$ was the first QSL to be proposed that was unlike those in the OHLSM theorem[19]. The

thirteen 4f electrons of the Yb^{3+} ion form the spin–orbit-entangled Kramers doublets that are split by the D_{3d} crystal electric fields[20–22]. At temperatures considerably lower than the crystal field gap (about 420 K), the magnetic properties of YbMgGaO$_4$ are captured by the ground-state doublet that is described by an effective spin-1/2 local moment; this is confirmed by a measured magnetic entropy of $R\ln(2)$ per Yb^{3+} ion[18], where R is the ideal gas constant. Figure 1a, b shows that the YbO$_6$ octahedra form well-separated triangular layers. Because of the large difference in chemistry between Yb^{3+} and the non-magnetic Mg^{2+}/Ga^{3+} ions, intra-triangular-layer impurities are prevented in YbMgGaO$_4$ (refs 18, 19, 21). Hence, the Yb system is a spin-1/2 antiferromagnet on a perfect triangular lattice.
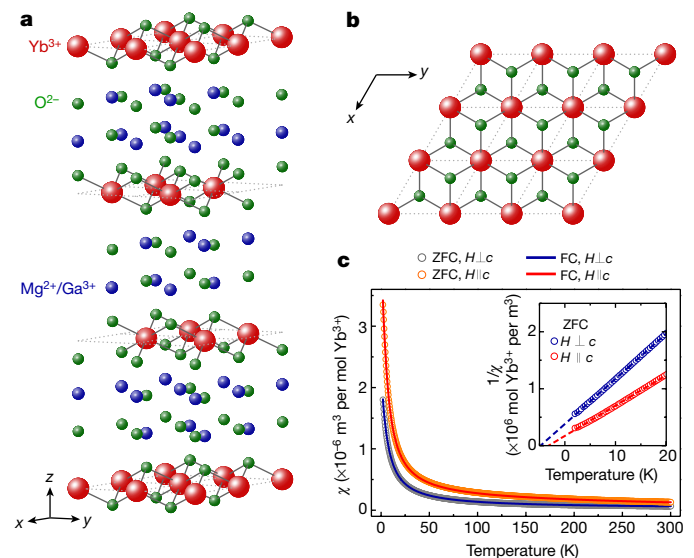

Figure 1 | Crystal structure and magnetic susceptibility of a single crystal of YbMgGaO$_4$. a, Schematic of the YbMgGaO$_4$ crystal structure. The dashed line indicates the unit cell. **b**, A triangular layer of Yb^{3+} ions and oxygen. **c**, Direct-current magnetic susceptibility χ measured under zero-field cooling (ZFC) and field cooling (FC) for single crystals of YbMgGaO$_4$, under magnetic fields ($H = 1$ T) applied perpendicular and parallel to the c axis. Paramagnetic behaviour is observed at low temperature with no obvious differences between ZFC and FC data. The inset shows the inverse susceptibility $1/\chi$ at low temperature (≤ 20 K), fitted with the Curie–Weiss law (dashed line). The fitting results in Curie temperatures of $\Theta_{CW,\perp} = -4.78$ K and $\Theta_{CW,\parallel} = -3.2$ K for perpendicular and parallel magnetic fields, respectively.

[1]State Key Laboratory of Surface Physics and Department of Physics, Fudan University, Shanghai 200433, China. [2]School of Computer Science, Fudan University, Shanghai 200433, China. [3]Department of Physics, Beijing Key Laboratory of Opto-electronic Functional Materials and Micro-nano Devices, Renmin University of China, Beijing 100872, China. [4]ISIS Facility, Rutherford Appleton Laboratory, STFC, Chilton, Didcot OX11 0QX, UK. [5]Institut Laue-Langevin, 71 Avenue des Martyrs, 38042 Grenoble Cedex 9, France. [6]Helmholtz-Zentrum Berlin für Materialien und Energie, D-14109 Berlin, Germany. [7]NIST Center for Neutron Research, National Institute of Standards and Technology, Gaithersburg, Maryland 20899, USA. [8]Quantum Condensed Matter Division, Oak Ridge National Laboratory, Oak Ridge, Tennessee 37831-6393, USA. [9]Neutron Scattering Laboratory, China Institute of Atomic Energy, Beijing 102413, China. [10]Department of Physics and Astronomy, Shanghai Jiao Tong University, Shanghai 200240, China. [11]Collaborative Innovation Center of Advanced Microstructures, Nanjing 210093, China. [12]Center for Field Theory and Particle Physics, Fudan University, Shanghai 200433, China.
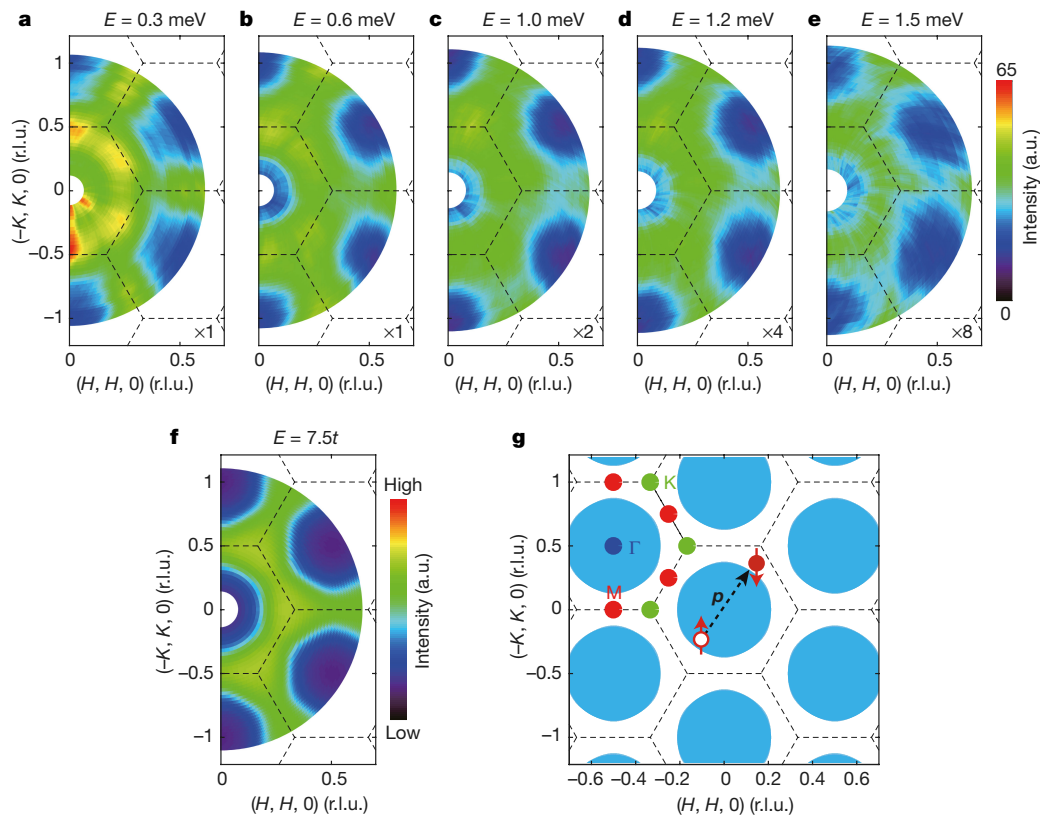
Figure 2 | Measured and calculated momentum dependence of the spin excitations, and calculated spinon Fermi surface of YbMgGaO$_4$.
a–**e**, Constant-energy images at the indicated energies and $T = 70$ mK, displaying diffusive magnetic excitations covering a wide region of the Brillouin zone. The scattering intensity is represented by the colour scale, and in **c**, **d** and **e** has been multiplied by 2, 4 and 8, respectively, for clarity. The data were collected on ThALES using the Flatcone detector, and were corrected for neutron-beam self-attenuation (Methods). **f**, Calculated momentum dependence of the spin excitations for a typical, finite E.

Here t is the hopping amplitude between nearest-neighbour sites. **g**, Spinon Fermi surface calculated using the model described in the main text. The black arrow indicates a spinon particle–hole excitation with momentum transfer $\boldsymbol{p}$ and dashed lines indicate the Brillouin zone boundaries of the conventional unit cell ($a = b = 3.40$ Å, $c = 25.12$ Å). High-symmetry points M, K and Γ are labelled by red, green and blue dots, respectively. The wave vector $\boldsymbol{Q}$ is defined as $\boldsymbol{Q} = H\boldsymbol{a}^* + K\boldsymbol{b}^* + L\boldsymbol{c}^*$; a.u., arbitrary units; r.l.u., reciprocal lattice units.

To characterize the behaviour of the local moment of Yb, we first measured the magnetic susceptibility of single-crystalline YbMgGaO$_4$ (Fig. 1c). For magnetic fields H applied both parallel to and normal to the c axis of the lattice, we found predominantly antiferromagnetic spin interactions, as evidenced by negative Curie–Weiss temperatures (Fig. 1c, inset). Because of the anisotropic spin interaction, the Curie–Weiss temperatures for $H \perp c$ and $H \parallel c$ were not identical (Fig. 1c, inset; Extended Data Fig. 1f), with $\Theta_{CW,\perp} = -4.78$ K and $\Theta_{CW,\parallel} = -3.2$ K, consistent with previous measurements[18,19]. We examined the magnetic susceptibilities in field cooling (FC) and zero-field cooling (ZFC) measurements. No splitting was detected between the FC and ZFC results down to 2 K, indicating the absence of spin glassy transitions (Fig. 1c).

The Curie–Weiss temperature and the spin excitation bandwidth (discussed below) set the energy scale for the spin interactions. Our elastic neutron scattering measurements revealed no magnetic Bragg peaks (Extended Data Fig. 2) at temperatures as low as 30 mK, considerably lower than the Curie–Weiss temperature (about 4 K) and spin excitation bandwidth (about 17 K); this is consistent with previous measurements of specific heat and susceptibility. To reveal the intrinsic quantum dynamics of the local moments of Yb, we used inelastic neutron scattering (INS) to study the spin excitations in single crystals of YbMgGaO$_4$ at approximately 70 mK. Constant-energy images are presented in Fig. 2a–e, which indicate the presence of diffusive magnetic excitations for all measured energies. The scattering spectral weights are spread broadly in the Brillouin zone, whereas the spectral intensities near the zone centre (that is, the Γ point) are suppressed. For a low-energy transfer of 0.3 meV, the spectral intensity

is slightly more pronounced around the M points, while the broad continuum across the Brillouin zone still carries the vast majority of the spectral weight (Fig. 2a).

Figure 3a displays a contour plot of spectral intensity along the high-symmetry momentum directions (M–K–Γ–M–Γ) in energy–momentum (E–$\boldsymbol{Q}$) space. Similarly to the constant-energy images shown in Fig. 2a–e, the spectral intensity is broadly distributed in momentum for all of the energies measured. Moreover, a clear V-shaped upper bound on the excitation energy is evident near the Γ point (Fig. 3a, dotted line). The intensity of the spin excitation gradually decreases with increasing energy, and vanishes above approximately 1.5 meV. This feature is confirmed by the $\boldsymbol{Q}$ scans in Fig. 4a, b and the E scans at a few given momentum points (Γ, M and K) in Fig. 4c.

The broad continuum is an immediate consequence, and strong evidence, of spinon excitations in QSLs[1,7,12]. This differs from magnon-like excitations that would peak strongly at specific momenta in reciprocal space, with or without static magnetic order[23,24]. In general, the spinful excitations in QSLs are carried by deconfined spinons[1,7]. For most experimentally relevant QSLs, the spinons carry half-integer spins. One neutron-spin-flip event in an INS measurement creates an integer spin change that necessarily excites two (or more) spinons[1]. Therefore, the energy transfer E and momentum transfer $\boldsymbol{p}$ of the neutron are shared by two spinon excitations that are created by the neutron spin flip. According to energy–momentum conservation, we have $E(\boldsymbol{p}) = \omega_s(\boldsymbol{k}) + \omega_s(\boldsymbol{p} - \boldsymbol{k})$, where $\omega_s(\boldsymbol{k})$ is the spinon dispersion and $\boldsymbol{k}$ is the momentum of one spinon. This relation implies the presence of an excitation continuum in the INS spectrum. The broad
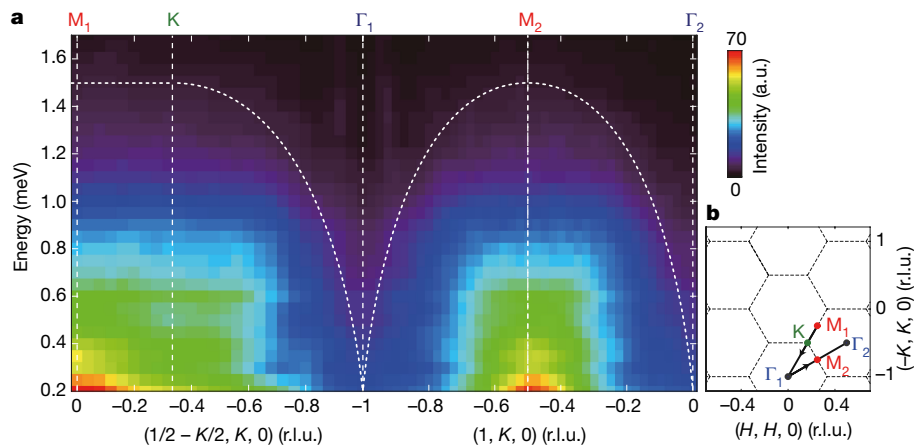
Figure 3 | Intensity of the spin-excitation spectrum along the high-symmetry momentum directions. a, Contour plot of the intensity along the $(1/2 - K/2, K, 0)$ and $(1, K, 0)$ directions illustrated by the black lines in **b**. The y axis represents the energy transfer. Vertical dashed lines represent the high-symmetry points and dotted lines indicate the upper bounds on the energy of the spin excitations. **b**, Sketch of reciprocal space. Dashed lines indicate the Brillouin zone boundaries.

continua in Figs 2a–e and 3a at different energies are as expected for the continuum excitations of two spinons.

The broad neutron-scattering spectral intensity that persists to the lowest energy that we measured suggests a high density of spinon scattering states at low energies. This cannot be explained by a Dirac QSL[2,25], in which the spectral continuum at low energies would concentrate near a few discrete momenta that connect the Dirac cones (Methods), or by any simple gapped QSL. Because of the gap, the spectral intensity would exceed a specified energy threshold. Even if the gap was smaller than the lowest measured energy, the spinon excitations would, except under special circumstances[16], occupy only one or a few discrete spots in reciprocal space at low energies[26], gradually expanding with increasing energy; a broad continuum at all energies and diminishing spectral weight at Γ (Fig. 3a) would not be observed. Moreover, Dirac and gapped QSLs are inconsistent with the observed low-temperature sublinear power-law behaviour of the heat capacity[19]. In contrast, the spinon-Fermi-surface QSL, with a high density of spinon states near the spinon Fermi surface, provides a consistent explanation for the INS results of YbMgGaO$_4$.

To account for these possible QSL signatures in YbMgGaO$_4$, we consider a minimal mean-field spinon Hamiltonian with a uniform spinon hopping on the triangular lattice. With a zero background flux for the spinons, the spinons form a large Fermi surface in the Brillouin zone (Fig. 2g). Although the anisotropic spin exchange caused by the spin–orbit coupling[19–21] breaks the spin-rotational symmetry of this simple model, the mean-field state considered here captures the essential properties of the spinon-Fermi-surface QSL in this system. For this spinon Fermi surface state, one neutron spin flip excites one spinon particle–hole pair across the Fermi surface. Therefore, the dynamic spin structure factor $\mathcal{S}(\boldsymbol{p}, E)$, measured by INS, directly probes the spinon particle–hole excitations across the spinon Fermi surface (Fig. 2g).

For low E, a minimum momentum transfer $p_{\min} \approx E/v_F$, where v_F is the Fermi velocity, is required to excite the spinon particle–hole pairs. Therefore, the spectral intensity near the Γ point should be gradually suppressed with increasing energy, leading to an upper bound on the excitation energy near the Γ point, as is clearly observed in Fig. 3a (V-shaped dotted line). For a typical, finite E, the calculated spectrum based on the spinon particle–hole continuum is shown in Fig. 2f. This spectrum is qualitatively consistent with the experimental observation of the broad spinon continuum in reciprocal space. Finally, when E exceeds the spinon bandwidth, the single spinon particle–hole excitation process is suppressed, and the spinon excitation intensity is suppressed accordingly. This feature is consistent with the vanishing of the spectral intensity above about 1.5 meV (dotted line) seen in Figs 3a and 4c. Therefore, we propose that YbMgGaO$_4$ is a QSL with a spinon Fermi surface.

The spinon Fermi surface alone has a constant density of states and would give a heat capacity that depends linearly on temperature ($C_v \propto T$). To account for the $C_v \propto T^{2/3}$ behaviour in YbMgGaO$_4$[19], we further propose that the candidate QSL is a spinon-Fermi-surface U(1) QSL, where the strong U(1) gauge fluctuation invokes a self-energy
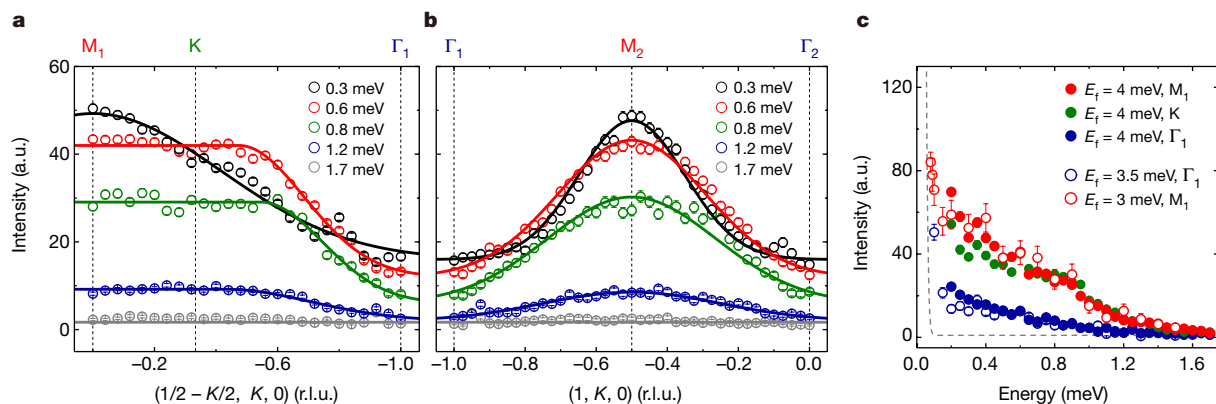

Figure 4 | Constant-energy scans along the symmetry directions and constant-Q scans at the high-symmetry points. a, b, Constant-energy scans along the $(1/2 - K/2, K, 0)$ and $(1, K, 0)$ directions. The solid lines are guides to the eye. **c**, Constant-Q scans at the M, K and Γ points with the final energy E_f fixed at 3 meV, 3.5 meV and 4 meV, as indicated. The sharp upturn of the scattering below about 0.1 meV is due to contamination from incoherent elastic scattering at $E = 0$ meV (dashed line, $E_f = 3$ meV). Error bars, 1 s.d.

correction in the spinons, thus enhancing the low-energy density of states[27–29].

During the review of the Letter, a related preprint[30] appeared that discusses the role of the next-nearest-neighbour interaction in the formation of the QSL state in YbMgGaO$_4$.

1. Balents, L. Spin liquids in frustrated magnets. *Nature* **464,** 199–208 (2010).
2. Wen, X.-G. Quantum orders and symmetric spin liquids. *Phys. Rev. B* **65,** 165113 (2002).
3. Kivelson, S. A., Rokhsar, D. S. & Sethna, J. P. Topology of the resonating valence-bond state: solitons and high-T_c superconductivity. *Phys. Rev. B* **35,** 8865(R)–8868(R) (1987).
4. Anderson, P. W. Resonating valence bonds: a new kind of insulator? *Mater. Res. Bull.* **8,** 153–160 (1973).
5. Anderson, P. W. The resonating valence bond state in La$_2$CuO$_4$ and superconductivity. *Science* **235,** 1196–1198 (1987).
6. Moessner, R. & Sondhi, S. L. Resonating valence bond liquid physics on the triangular lattice. *Prog. Theor. Phys.* **145** (Suppl.), 37–42 (2002).
7. Lee, P. A. An end to the drought of quantum spin liquids. *Science* **321,** 1306–1307 (2008).
8. Kurosaki, Y., Shimizu, Y., Miyagawa, K., Kanoda, K. & Saito, G. Mott transition from a spin liquid to a Fermi liquid in the spin-frustrated organic conductor κ-(ET)$_2$Cu$_2$(CN)$_3$. *Phys. Rev. Lett.* **95,** 177001 (2005).
9. Itou, T., Oyamada, A., Maegawa, S., Tamura, M. & Kato, R. Quantum spin liquid in the spin-1/2 triangular antiferromagnet EtMe$_3$Sb[Pd(dmit)$_2$]$_2$. *Phys. Rev. B* **77,** 104413 (2008).
10. Shimizu, Y., Miyagawa, K., Kanoda, K., Maesato, M. & Saito, G. Spin liquid state in an organic Mott insulator with a triangular lattice. *Phys. Rev. Lett.* **91,** 107001 (2003).
11. Coldea, R., Tennant, D. A. & Tylczynski, Z. Extended scattering continua characteristic of spin fractionalization in the two-dimensional frustrated quantum magnet Cs$_2$CuCl$_4$ observed by neutron scattering. *Phys. Rev. B* **68,** 134424 (2003).
12. Han, T.-H. *et al.* Fractionalized excitations in the spin-liquid state of a kagome-lattice antiferromagnet. *Nature* **492,** 406–410 (2012).
13. Oshikawa, M. Commensurability, excitation gap, and topology in quantum many-particle systems on a periodic lattice. *Phys. Rev. Lett.* **84,** 1535–1538 (2000).
14. Hastings, M. B. Lieb–Schultz–Mattis in higher dimensions. *Phys. Rev. B* **69,** 104431 (2004).
15. Lieb, E., Schultz, T. & Mattis, D. Two soluble models of an antiferromagnetic chain. *Ann. Phys.* **16,** 407–466 (1961).
16. Punk, M., Chowdhury, D. & Sachdev, S. Topological excitations and the dynamic structure factor of spin liquids on the kagome lattice. *Nat. Phys.* **10,** 289–293 (2014).
17. Watanabe, H., Po, H. C., Vishwanath, A. & Zaletel, M. Filling constraints for spin–orbit coupled insulators in symmorphic and nonsymmorphic crystals. *Proc. Natl Acad. Sci. USA* **112,** 14551–14556 (2015).
18. Li, Y. *et al.* Gapless quantum spin liquid ground state in the two-dimensional spin-1/2 triangular antiferromagnet YbMgGaO$_4$. *Sci. Rep.* **5,** 16419 (2015).
19. Li, Y. *et al.* Rare-earth triangular lattice spin liquid: a single-crystal study of YbMgGaO$_4$. *Phys. Rev. Lett.* **115,** 167203 (2015).
20. Li, Y.-D., Wang, X. & Chen, G. Anisotropic spin model of strong spin–orbit-coupled triangular antiferromagnets. *Phys. Rev. B* **94,** 035107 (2016).
21. Li, Y.-D., Shen, Y., Li, Y., Zhao, J. & Chen, G. The effect of spin–orbit coupling on the effective-spin correlation in YbMgGaO$_4$. Preprint at http://arxiv.org/abs/1608.06445 (2016).
22. Ross, K. A., Savary, L., Gaulin, B. D. & Balents, L. Quantum excitations in quantum spin ice. *Phys. Rev. X* **1,** 021002 (2011).
23. Zhao, J. *et al.* Neutron scattering measurements of spatially anisotropic magnetic exchange interactions in semiconducting K$_{0.85}$Fe$_{1.54}$Se$_2$ (T_N = 280 K). *Phys. Rev. Lett.* **112,** 177002 (2014).
24. Wang, Q. *et al.* Magnetic ground state of FeSe. *Nat. Commun.* **7,** 12182 (2016).
25. Ran, Y., Hermele, M., Lee, P. A. & Wen, X.-G. Projected-wave-function study of the spin-1/2 Heisenberg model on the Kagomé lattice. *Phys. Rev. Lett.* **98,** 117205 (2007).
26. Sachdev, S. Kagomé- and triangular-lattice Heisenberg antiferromagnets: ordering from quantum fluctuations and quantum-disordered ground states with unconfined bosonic spinons. *Phys. Rev. B* **45,** 12377–12396 (1992).
27. Lee, S.-S. & Lee, P. A. U(1) gauge theory of the Hubbard model: spin liquid states and possible application to κ-(BEDT-TTF)$_2$Cu$_2$(CN)$_3$. *Phys. Rev. Lett.* **95,** 036403 (2005).
28. Motrunich, O. I. Variational study of triangular lattice spin-1/2 model with ring exchanges and spin liquid state in κ-(ET)$_2$Cu$_2$(CN)$_3$. *Phys. Rev. B* **72,** 045105 (2005).
29. Lee, P. A. & Nagaosa, N. Gauge theory of the normal state of high-T_c superconductors. *Phys. Rev. B* **46,** 5621–5639 (1992).
30. Paddison, J. A. M. *et al.* Continuous excitations of the triangular-lattice quantum spin liquid YbMgGaO$_4$. Preprint at http://arxiv.org/abs/1607.03231 (2016).

Author Contributions J.Z. and G.C. planned the project. Y.S., H.W. and S.S. synthesized the sample. Y.S. and Y.H. characterized the sample with the help of Y.L. and Q.Z. Y.S., H.W., S.S., B.P., Q.W., H.C.W., P.S. and J.Z. carried out the neutron experiments with experimental assistance from M.B., D.L.Q.-C., L.W.H., L.H., M.D.F. and S.M. J.Z. and Y.S. analysed the data. Y.-D.L. and G.C. provided the theoretical explanation and calculations. J.Z., G.C., Y.S. and Y.-D.L. wrote the paper. All authors provided comments on the paper.

Author Information Reprints and permissions information is available at www.nature.com/reprints. The authors declare no competing financial interests. Readers are welcome to comment on the online version of the paper. Correspondence and requests for materials should be addressed to J.Z. (zhaoj@fudan.edu.cn) or G.C. (gchen_physics@fudan.edu.cn).

Reviewer Information *Nature* thanks C. Rüegg and the other anonymous reviewer(s) for their contribution to the peer review of this work.

METHODS

Sample growth and characterizations. High-quality YbMgGaO$_4$ single crystals were synthesized using the optical floating zone technique[19]. A representative single crystal, which is optically transparent with mirror-like cleaved surfaces, is shown in Extended Data Fig. 1a. Our X-ray diffraction (XRD) measurements revealed that all of the reflections from the cleaved surface could be indexed by (0, 0, L) peaks of triangular YbMgGaO$_4$; no impurity phases were observed (Extended Data Fig. 1b). The full-width at half-maximum (FWHM) of the rocking curve of the (0, 0, 18) peak was about 0.009°, indicating an extremely high crystallization quality (Extended Data Fig. 1c). This was confirmed by the sharp and clear diffraction spots in the X-ray Laue pattern (Extended Data Fig. 1d). Powder XRD patterns on ground single crystals also revealed no indication of impurity phases (Extended Data Fig. 1e). The Rietveld refinements[31] confirm that the XRD pattern can be described by the $R\bar{3}m$ space group. The refined structural parameters are given in Extended Data Table 1. These results suggested that the YbMgGaO$_4$ single crystal possessed a perfect triangular lattice with no detectable impurities. This is consistent with previous measurements that have demonstrated that the impurity/isolated spins are less than 0.04% in similar samples[18,19]. Although the Mg/Ga site disorder in the non-magnetic layers does not directly affect the exchange interaction between the Yb local moments, it may have an indirect effect and could lead to some exchange disorder. It seems that this disorder is not significant, because no signs of spin freezing were observed. A QSL is often stable against weak local perturbations, provided that the perturbation is irrelevant or not significant. Therefore, if a QSL is realized as the ground state for YbMgGaO$_4$, then the possible exchange disorder will not destabilize this state if the disorder strength is not significant.

In addition, the field dependence of magnetization in our single crystal displayed a linear behaviour above 12 T (Extended Data Fig. 1f), indicative of a fully polarized state. The Van Vleck susceptibility extracted from the linear-field-dependent magnetization data was subtracted in the inset of Fig. 1c.

Neutron scattering experiments. INS measurements were carried out on the ThALES cold triple-axis spectrometer at the Institut Laue-Langevin, Grenoble, France, and at the FLEXX cold triple-axis spectrometer in the BER-II reactor at Helmholtz-Zentrum Berlin, Germany[32]. For the ThALES experiment, silicon (111) was used as a monochromator and analyser; the final neutron energies were fixed at $E_f = 3$ meV (energy resolution of about 0.05 meV), $E_f = 3.5$ meV (energy resolution of about 0.08 meV) or $E_f = 4$ meV (energy resolution of about 0.1 meV). For the FLEXX experiment, pyrolythic graphite (002) was used as a monochromator and analyser. Contamination from higher-order neutrons was eliminated through a velocity selector installed in the front of the monochromator. The final neutron energy was fixed at $E_f = 3.5$ meV (energy resolution of about 0.09 meV). Three (six) pieces of single crystals with total a mass of about 5 g (19 g) were coaligned in the (HK0) scattering plane for the ThALES (FLEXX) experiment. The FWHM of the rocking curve of the coaligned crystals for the ThALES and FLEXX experiments were approximately 0.95° and 0.92°, respectively. The elastic neutron scattering experiment was carried out at the WAND neutron diffractometer at the High Flux Isotope Reactor, Oak Ridge National Laboratory, USA; one single crystal was used for the experiment, with the incident wavelength $\lambda = 1.488$ Å (Extended Data Fig. 2). For the low-temperature experiments, a dilution insert for the standard ^{4}He cryostat was used to reach temperatures down to around 30–70 mK.

Because of the non-uniform shape of the single crystal, the relatively large sample volume and the extremely broad spin-excitation spectrum, the neutron beam self-attenuation (by the sample) may require consideration. In most cases the self-attenuation is dependent on only the distance traversed by the neutrons through the sample. We observed the self-attenuation effect in an elastic incoherent scattering image of our sample at 20 K, which exhibited an anisotropic intensity distribution (Extended Data Fig. 3a). The self-attenuation effect was also observed in the raw constant-energy images (Extended Data Fig. 3b–f), which were shown to be anisotropic, with slightly higher intensities occurring at approximately the same direction as that observed in the elastic incoherent scattering images. The self-attenuation can be corrected by normalizing the data with the elastic incoherent scattering image; that is, the elastic incoherent scattering intensity, which is dependent on the sample position (ω) and scattering angle (2θ), is converted to a linear attenuation correction factor for the scattering images measured at different energies. The normalized constant-energy images are presented in Fig. 2a–e, revealing a nearly isotropic intensity distribution.

Extended Data Fig. 4 shows the spin excitation spectrum at 20 K, which is broadened and weakened compared with that at 70 mK (discussed below).

Spinon Fermi surface and dynamic spin structure factor. Here we explain the spinon mean-field state that is used to explain the dynamic spin structure factor of the neutron scattering experiments. As we proposed in the main text, a QSL with a spinon Fermi surface gives a compatible explanation for the INS results for YbMgGaO$_4$.

To describe the candidate spinon-Fermi-surface QSL state in YbMgGaO$_4$, we formally express the Yb^{3+} effective spin as the bilinear combination of the fermionic spinon with spin $S_i = \sum_{\alpha\beta} \frac{1}{2} f_{i\alpha}^\dagger \sigma_{\alpha\beta} f_{i\beta}$ and a Hilbert space constraint $\sum_\alpha f_{i\alpha}^\dagger f_{i\alpha} = 1$, where $\sigma_{\alpha\beta}$ is a vector whose three components are the Pauli matrices and $f_{i\alpha}^\dagger$ ($f_{i\alpha}$) creates (annihilates) a spinon with spin $\alpha = \uparrow, \downarrow$ at site i. For the QSL with a spinon Fermi surface, we propose a minimal mean-field Hamiltonian H_{MFT} for the spinons on the triangular lattice. We consider a uniform spinon hopping with a zero background flux:

$$H_{\text{MFT}} = -t\sum_{\langle ij\rangle} (f_{i\alpha}^\dagger f_{j\alpha} + \text{h.c.}) - \mu\sum_i f_{i\alpha}^\dagger f_{i\alpha} \qquad (1)$$

where t is the mean-field parameter, which represents the hopping amplitude between nearest-neighbour sites. The chemical potential μ is included to impose the Hilbert space constraint on average. Here, we have treated the spinons freely by neglecting the gauge fluctuations. This mean-field state gives a single spinon dispersion

$$\omega_k = -t\sum_{\{a_i\}} \cos(k \cdot a_i) - \mu$$

where $\{a_i\}$ are six nearest-neighbour vectors of the triangular lattice. Owing to the Hilbert space constraint, the spinon band is half-filled, leading to a large Fermi surface in the Brioullin zone (Extended Data Fig. 5a).

INS measures the dynamic spin structure factor

$$S(p, E) = \frac{1}{N}\sum_{i,j} e^{ip\cdot(r_i - r_j)} \int e^{-iEt} \langle S_i^-(t) \cdot S_j^+(0)\rangle dt$$
$$= \sum_n \delta(E - [E_n(p) - E_0]) \left|\langle n|S_p^+|\Omega\rangle\right|^2 \qquad (2)$$

where N is total number of lattice sites, the summation goes over all eigenstates, $|\Omega\rangle$ refers to the spinon ground state with the spinons filling the Fermi sea, E_0 is the energy of the ground state and $E_n(p)$ is the energy of the nth excited state with momentum p. In the actual calculation, owing to the energy resolution of the experiments, the δ function is taken to have a broadening:

$$\delta(E - \epsilon) = \frac{\eta/\pi}{(E - \epsilon)^2 + \eta^2}$$

where η is the broadening and ϵ is the measured energy. Because $S_p^+ = \sum_k f_{k+p\uparrow}^\dagger f_{k\downarrow}$, the summation in equation (2) would be over all possible spin-1 excited states that are characterized by one spinon particle–hole pair crossing the spinon Fermi surface (Fig. 2g) with a total momentum p and a total energy E. As we show in Fig. 2f and Extended Data Fig. 5b, and discuss in the main text, this spinon-Fermi-surface QSL state gives the three crucial features of the INS results: (1) the broad continuum that covers the large portion of the Brioullin zone; (2) the broad continuum persisting from the lowest energy transfer to the highest energy transfer; and (3) the clear upper excitation edge near the Γ point.

In our calculation of Fig. 2f and Extended Data Fig. 5b, we choose the lattice size to be 40×40 and $\eta = 1.2t$, in accordance with the energy and momentum resolution of the instruments. The energy scale of Fig. 2f is set to be $7.5t$.

Here we explain the details of the dynamic spin structure factor in Fig. 2f and Extended Data Fig. 5b, based on the particle–hole excitation of the spinon Fermi surface. For an infinitesimal energy transfer, the neutrons simply probe the spinon Fermi surface. Because the spinon particle and hole can be excited anywhere near the Fermi surface, the neutron spectral intensity appears from $p = 0$ to $p = 2k_F$, where k_F is the Fermi wavevector. Because $|2k_F|$ already exceeds the first Brillouin zone, the neutron spectral intensity then covers the whole Brillouin zone including the Γ point. For a small but finite E, as we explain in the main text, a minimal momentum transfer $p_{\min} \approx E/v_F$ is required to excite the spinon particle–hole pairs. Therefore, the spectral intensity gradually moves away from the Γ point as E increases. Because it is always possible to excite the spinon particle–hole pair with the momenta near the zone boundary, the spectral intensity is not greatly affected at the zone boundary as E increases. Thus, the broad continuum continues to cover a large portion of the Brillouin zone at a finite E.

With the free spinon mean-field model H_{MFT}, we further calculate the spectral weight along the energy direction for fixed momenta. The discrepancy between the theoretical results in Extended Data Fig. 5d and the experimental results in Extended Data Fig. 5e occurs at low energies. We attribute this low-energy discrepancy to the fact that the free spinon theory ignores the gauge fluctuations. The enhancement of the low-energy spectral weight compared to the free spinon results is then identified as possible evidence of strong gauge fluctuations in the system; we elaborate on this in the following discussion of the heat capacity behaviour.

To account for the heat capacity behaviour, we suggest that the candidate QSL is a spinon-Fermi-surface U(1) QSL. Here we elaborate on this point and discuss the U(1) gauge fluctuation of this state in detail. The stability of U(1) QSLs with a spinon Fermi surface against the spinon confinement has been addressed extensively[33,34]. It was proposed and understood that the large densities of gapless fermionic spinons on the spinon Fermi surface help to suppress the instanton events of the compact U(1) gauge field in two-dimensional U(1) QSLs[33,34]. The proliferation of instanton events is the cause of the gauge confinement of a U(1) lattice gauge theory for a U(1) QSL without gapless spinons[35]. Because the instanton event is suppressed here, the compactness of the U(1) gauge field is no longer an issue, and the low-energy property of our U(1) QSL is then described by gapless fermionic spinons coupled with a non-compact U(1) gauge field[27,33,36]. Owing to the coupling to the gapless spinons, the U(1) gauge photon is overly Landau damped and becomes very soft. The soft gauge photon strongly scatters the fermionic spinons, provides a self-energy correction to the Green's function of the spinon, and thus makes the quasi-particle weight for spinons equal to zero[27,29,33,36]. The resulting spinon non-Fermi liquid state has an enhanced density of low-energy spinon states that results in a sublinear power-law temperature dependence for the low-temperature heat capacity[27,29,33,36]. In addition to the heat capacity behaviour, we find that, owing to the spinon–gauge coupling and the U(1) gauge fluctuation, the enhanced density of the low-energy spinon states is consistent with the enhanced spectral intensities at low energies for the fixed momenta in Extended Data Fig. 5e.

The stability of the spinon non-Fermi liquid against spinon pairing has also been considered theoretically[37]. When the spinons pair up, similar to the Cooper pairing of electrons in a superconductor, the continuous part of the U(1) gauge field becomes massive, owing to the Anderson–Higgs mechanism, leaving the Z_2 part of the gauge field unaffected. The resulting state from the spinon pairing of a spinon-Fermi-surface U(1) QSL is a Z_2 QSL. Such a spinon pairing scenario was proposed to account for the very low-temperature behaviour of the organic spin liquid κ-(BEDT-TTF)$_2$Cu$_2$(CN)$_3$ (ref. 38). However, for YbMgGaO$_4$, we do not find any evidence of spinon pairings in either thermodynamic or spectroscopic measurements. Although the INS measurement might be constrained by the energy resolution, the thermodynamic measurement did not find any suppression of the density of states down to the lowest temperatures[18,19]. If the spinon pairing instability occurs for YbMgGaO$_4$, it must be at a much lower temperature or energy scale than those of current and previous experiments[18,19]. In any case, the presence of a spinon Fermi surface is the precondition for any spinon pairing instability.

We now discuss the finite-temperature thermal effect of the QSL. For the spinon-Fermi-surface U(1) QSL in two dimensions, there is no line-like object in the excitation spectrum. Therefore, as the temperature is increased from this QSL ground state, there is no thermal phase transition caused by proliferating any extended line-like excitations. Moreover, the spinon-Fermi-surface U(1) QSL is not characterized by any symmetry. Consequently, there is no symmetry-breaking transition as the temperature is increased. The absence of the thermal phase transition is consistent with what has been observed in YbMgGaO$_4$. As the temperature is increased from the $T = 0$ K ground state of the QSL, the system involves more thermal superposition of excited states and gradually loses its quantum coherence. A temperature of 20 K is approximately the energy scale of the spin excitation bandwidth, which sets the interaction energy scale between the Yb local moments. At this temperature, the correlation between the local moments cannot be ignored. Its consequence is the diffusive feature in the INS spectrum. This is consistent with our data measured

at 20 K shown in Extended Data Fig. 4a, b, in which the spectral weight becomes more diffusive.

Finally, we comment on the weak spectral peak at the M points at low energies (Figs 2a, 3a). This non-generic feature of the neutron spectrum is not obtained in the theoretical calculation using the minimal spinon mean-field model in equation (1). This is because we did not include the effect of anisotropic spin interaction, which would break the spin rotational symmetry of equation (1). In the strong anisotropic limit, the generic spin interaction for the Yb local moments favours stripe-like magnetic order, with the wavevectors at the M points[20]. In a recent calculation, it was shown that the anisotropic spin interaction enhances the spin correlation at the M points[21]. Despite the presence of a weak peak at M, the vast majority of the spectral weight is still dominated by a broad continuum across the Brillouin zone at the lowest energies measured (Figs 2a, 3a).

Dynamic spin structure factor of a Dirac QSL. As a comparison with the spinon-Fermi-surface QSL, we carry out the same calculation for the spinon mean-field Hamiltonian with a background π flux through each unit cell. This choice of the background flux gives a Dirac U(1) QSL. We fix the gauge according to the hopping parameters that are specified in Extended Data Fig. 6a. The spinon band structure of this mean-field Hamiltonian is

$$\omega_{\mathbf{k}} = \pm\sqrt{2}\,t\sqrt{3 + \cos(2k_x) + 2\sin(k_x)\sin(\sqrt{3}\,k_y)}$$

where we have set the lattice constant to unity. We observe two Dirac nodes at $\mathbf{k} = (\pm\pi/2, \mp\pi/(2\sqrt{3}))$ (Extended Data Fig. 6b); the spinon Fermi energy is right at the Dirac nodes.

At low energies, the only spin-1 excited states involve either an intra-Dirac-cone spinon particle–hole pair or an inter-Dirac-cone particle–hole pair. Therefore, the spectral intensity of the dynamic spin structure factor should be concentrated at the momentum transfer that corresponds to the intra-Dirac-cone and the inter-Dirac-cone processes. As shown Extended Data Fig. 6c, d, the dynamic spin structure factor at low energies is peaked at the Γ point, the M $= (0, 2\pi/\sqrt{3})$ point and the symmetry-equivalent momentum points. This result differs from the broad continuum that is observed in the experiment. Therefore, the π-flux state is inconsistent with the experimental data, as are other Dirac spin liquids.

Data availability. The data that support the findings of this study are available from the corresponding author on reasonable request.

31. Rodríguez-Carvajal, J. Recent advances in magnetic structure determination by neutron powder diffraction. *Physica B* **192,** 55–69 (1993).
32. Le, M. D. *et al.* Gains from the upgrade of the cold neutron triple-axis spectrometer FLEXX at the BER-II reactor. *Nucl. Instrum. Methods A* **729,** 220–226 (2013).
33. Lee, S. S. Stability of the U(1) spin liquid with a spinon Fermi surface in 2 + 1 dimensions. *Phys. Rev. B* **78,** 085129 (2008).
34. Hermele, M. *et al.* Stability of U(1) spin liquids in two dimensions. *Phys. Rev. B* **70,** 214437 (2004).
35. Polyakov, A. M. *Gauge Fields and Strings* Ch. 4 (Harwood Academic, 1987).
36. Lee, S. S. Low-energy effective theory of Fermi surface coupled with U(1) gauge field in 2 + 1 dimensions. *Phys. Rev. B* **80,** 165102 (2009).
37. Metlitski, M. A., Mross, D. F., Sachdev, S. & Senthil, T. Cooper pairing in non-Fermi liquids. *Phys. Rev. B* **91,** 115111 (2015).
38. Lee, S. S., Lee, P. A. & Senthil, T. Amperean pairing instability in the U(1) spin liquid state with Fermi surface and application to κ-(BEDT-TTF)$_2$Cu$_2$(CN)$_3$. *Phys. Rev. Lett.* **98,** 067006 (2007).
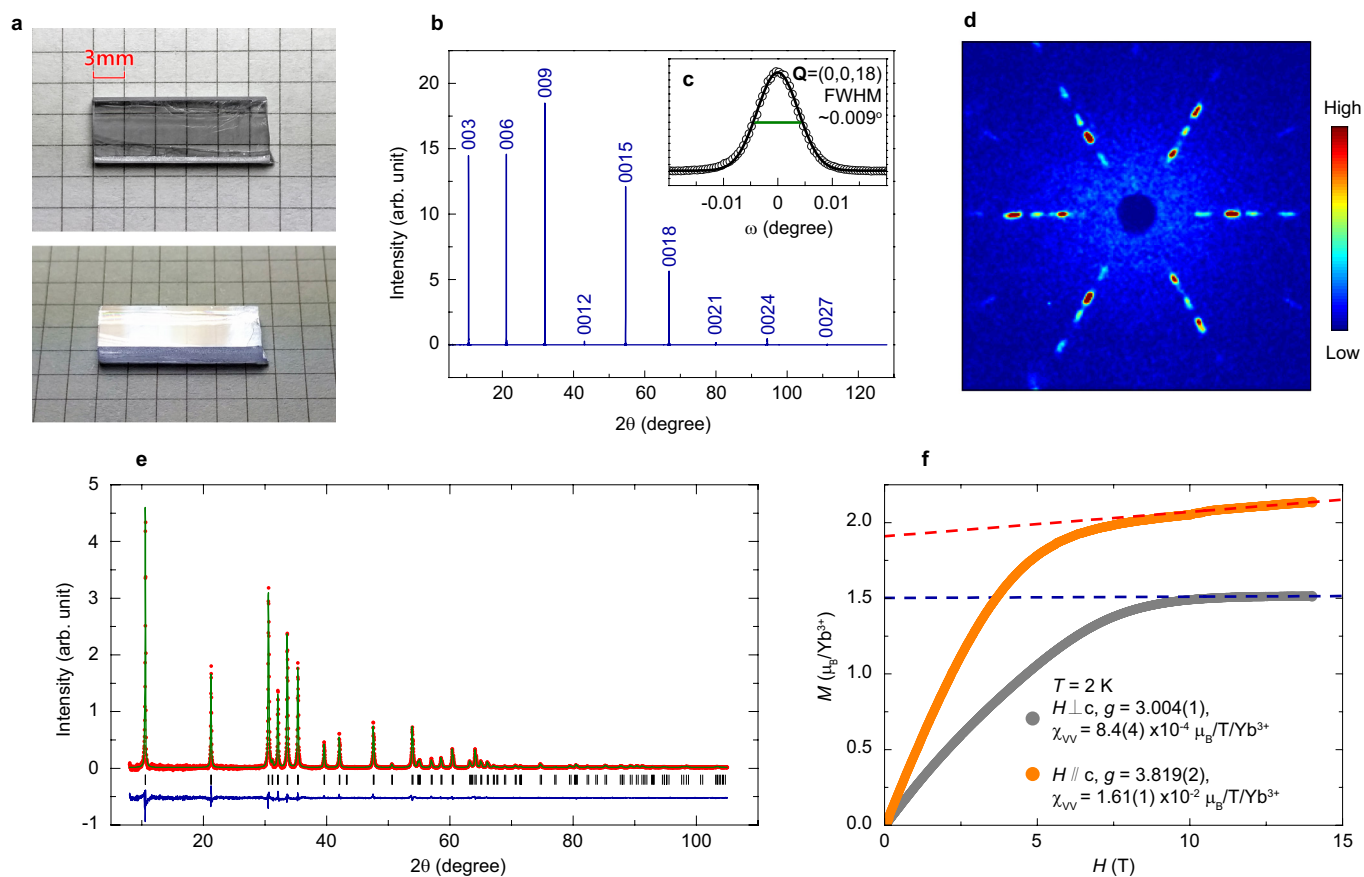
Extended Data Figure 1 | Photographs, XRD patterns and field dependence of the magnetization of YbMgGaO₄. a, Photographs of a representative YbMgGaO₄ single crystal. **b**, XRD pattern of a YbMgGaO₄ single crystal from the cleaved surface. **c**, Rocking curve of the (0, 0, 18) peak. The horizontal bar indicates the instrumental resolution. **d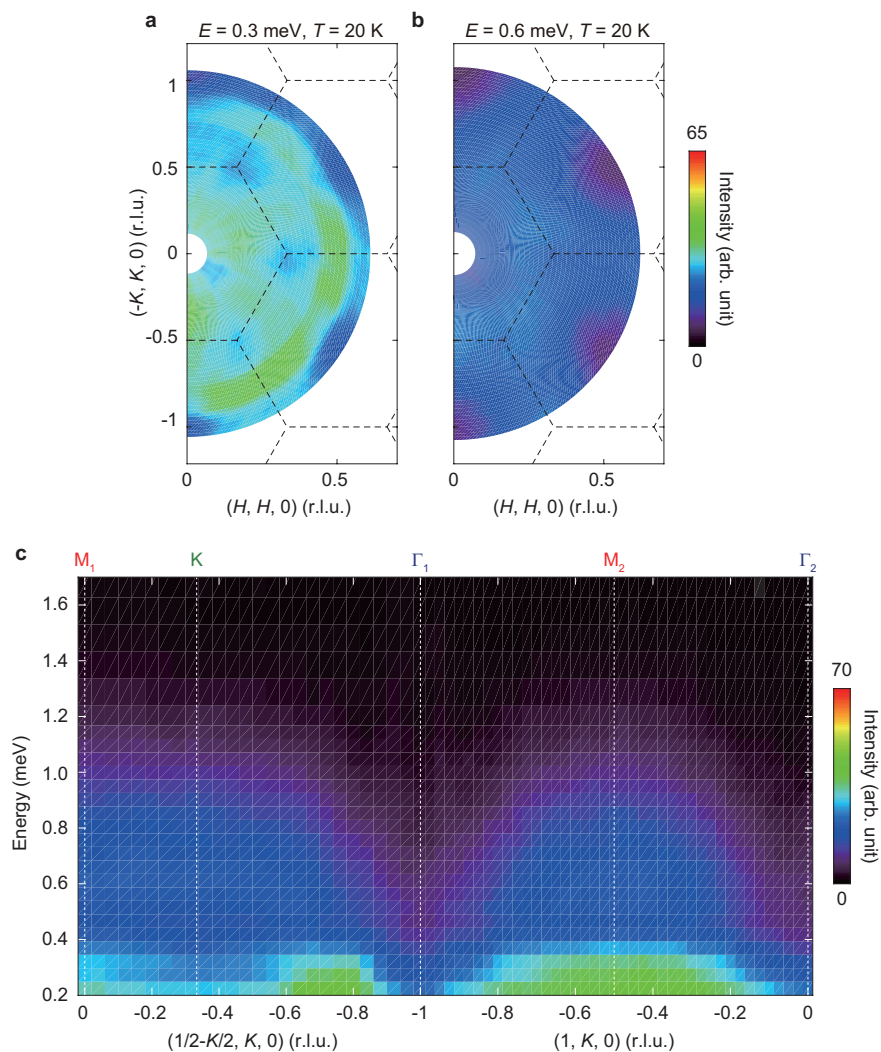**, Laue pattern of the YbMgGaO₄ single crystal viewed from the c axis. **e**, Observed (red) and calculated (green) XRD diffraction intensities of ground single crystals. The X-ray has a wavelength of 1.54 Å. The blue curve indicates the difference between the observed and calculated intensities. **f**, Magnetic field dependence of magnetization at $T = 2$ K. Fitted g factors and Van Vleck susceptibilities χ_{VV} are shown (μ_B is the Bohr magneton). The dashed lines are linear fits above 12 T.
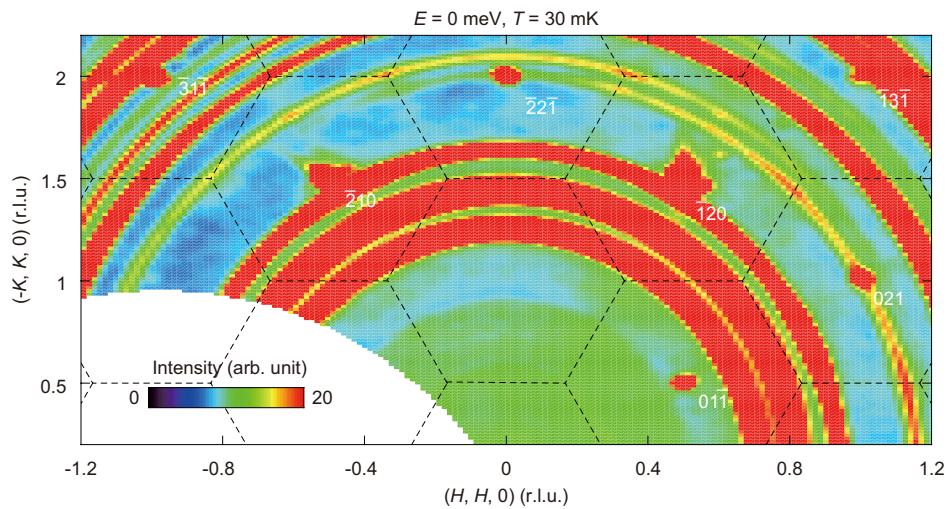
Extended Data Figure 2 | Elastic neutron scattering measurements . Elastic neutron scattering map in the $(HK0)$ plane at 30 mK. No magnetic Bragg peaks are observed. The ring-like pattern is due to scattering from the polycrystalline Cu and Al sample holder. Because of the very large c-axis lattice constant and a small tilt of the scattering plane, some of the tails of the nuclear Bragg peaks for $L = \pm 1$ can be also seen. Dashed lines indicate the Brillouin zone boundaries.

Extended Data Figure 3 | Correction of neutron beam self-attenuation. a, Elastic incoherent scattering image at 20 K. **b–f**, Raw constant-energy images at 70 mK and at the indicated energies. The scattering intensities in **d**, **e** and **f** have been multiplied by 2, 4 and 8, respectively, for clarity. Dashed lines indicate the Brillouin zone boundaries.

a $E = 0.3$ meV, $T = 20$ K

b $E = 0.6$ meV, $T = 20$ K

c

Extended Data Figure 4 | Additional neutron scattering data at 20 K. **a**, **b**, Constant-energy images at 0.3 meV (**a**) and 0.6 meV (**b**) at 20 K. **c**, Intensity contour plot of the spin excitation spectrum along the high-symmetry momentum directions at 20 K. The scattering is broadened and weakened compared with that at 70 mK.
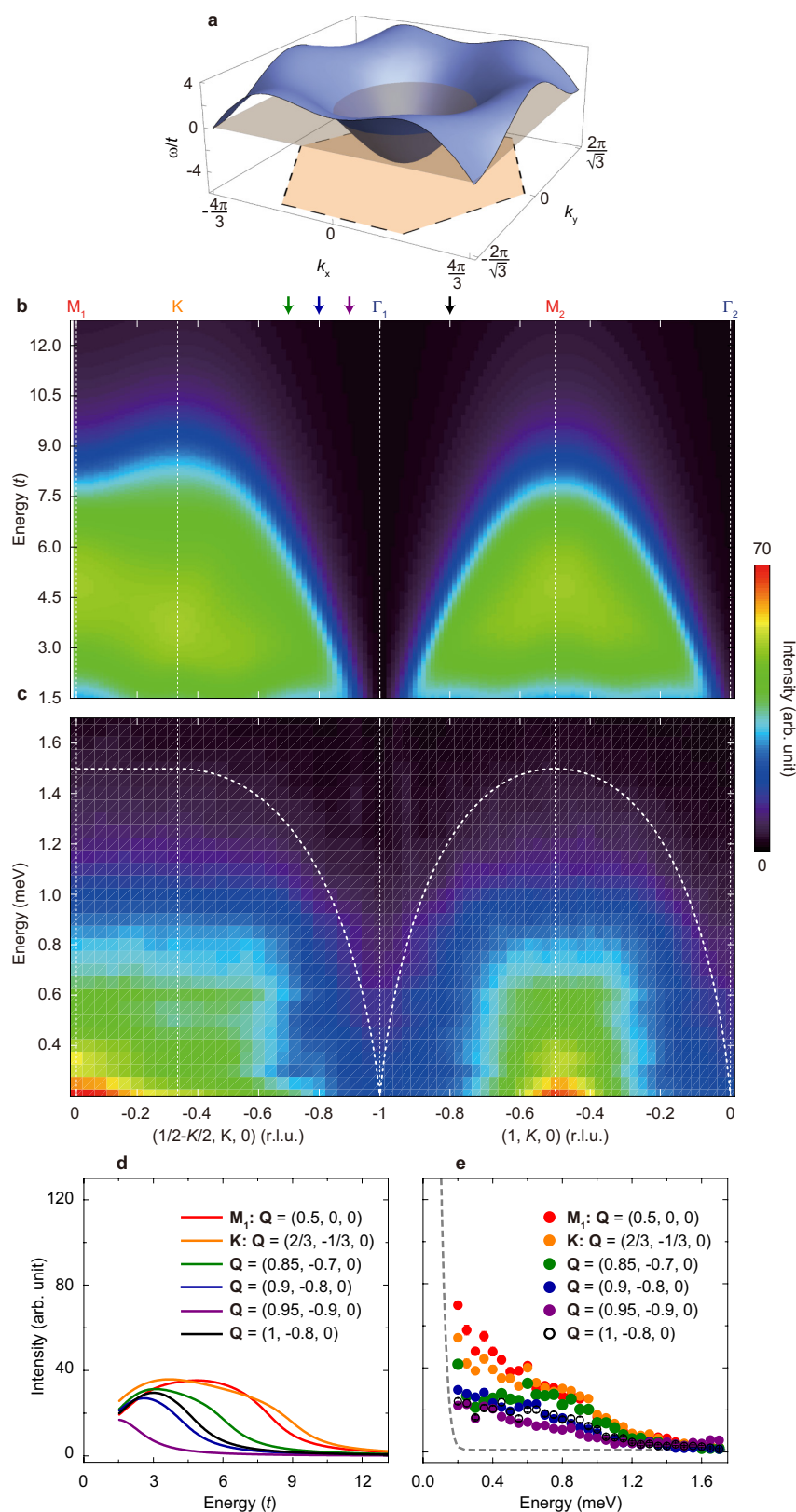
Extended Data Figure 5 | Calculation of the zero-flux Hamiltonian.
a, Spinon dispersion ω_k of the zero-flux Hamiltonian. The grey plane marks the Fermi level at $\omega = 0$; its intersection with the band gives the Fermi surface. The light orange hexagon represents the projection of the first Brillouin zone. The maximum of ω_k is $3t$ and the minimum is $-6t$, providing a bandwidth of $9t$. **b**, Calculated dynamic spin structure factor along high-symmetry directions. A reciprocal lattice unit (r.l.u.) is used

here, which is obtained using $H = k_x/(4\pi) - \sqrt{3}\,k_y/(4\pi)$ and $K = k_x/(4\pi) + \sqrt{3}\,k_y/(4\pi)$. **c**, Measured spin excitation spectrum along high-symmetry directions at 70 mK. **d**, Calculated energy dispersion at the indicated momenta (marked by arrows in **b**). **e**, Measured constant-Q scans at the indicated momenta. The dashed line is the incoherent elastic line for $E_f = 4$ meV.

a

b

c

$\omega = 2.1t$

d
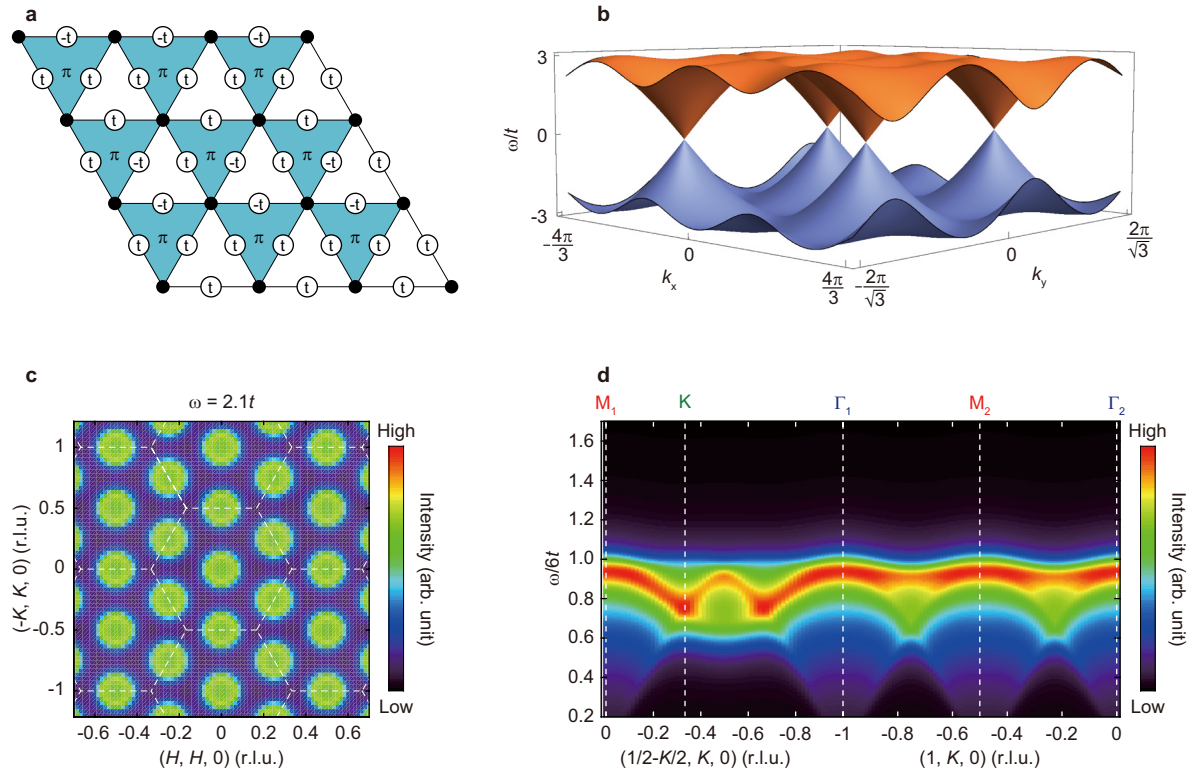
Extended Data Figure 6 | Calculation of the π-flux Hamiltonian. a, Flux pattern and real nearest-neighbour hoppings on the triangular lattice. In the figure, '+t' denotes $t_{ij} = t_{ji} = t$ and '−t' denotes $t_{ij} = t_{ji} = -t$; 'π' denotes triangles that are threaded by a π flux. b, Spinon band structure of the π-flux Hamiltonian. The two bands are particle–hole related, both with bandwidths of 3t. c, Calculated momentum dependence of the dynamic

spin structure factor at low energy $\omega = 2.1t$. Strong peaks can be distinguished at the Γ point, the M = (0, 2π/√3) point ((1/2, −1/2) in r.l.u.) and equivalent positions. White dashed lines denote the zone boundaries. d, Calculated dynamic spin structure factor along high-symmetry points with $\eta = 0.3t$.

Extended Data Table 1 | Refined structural parameters for YbMgGaO₄ at room temperature

	a (Å)	3.40125 (1)
	c (Å)	25.10632 (16)
Yb	B_{11} (Å²)	0.1332 (18)
	B_{33} (Å²)	0.00204 (3)
Mg	z	0.21378 (6)
	B_{11} (Å²)	0.131 (4)
	B_{33} (Å²)	0.00161 (6)
Ga	z	0.21378 (6)
	B_{11} (Å²)	1.131 (4)
	B_{33} (Å²)	0.00161 (6)
O1	z	0.28887 (19)
	B_{11} (Å²)	0.107 (9)
	B_{33} (Å²)	0.00226 (17)
O2	z	0.12884 (17)
	B_{11} (Å²)	0.137 (9)
	B_{33} (Å²)	0.00089 (18)
	Rp	1.18
	wRp	1.81
	χ^2	2.25

Space group: $R\bar{3}m$ (number 166). Atomic positions: Yb, 3a (0, 0, 0); Mg, 6c (0, 0, z); Ga, 6c (0, 0, z); O, 6c (0, 0, z). B_{ij}, Debye–Waller factor; Rp, profile factor; wRp, weighted profile factor.